AIP | Applied Physics Letters

Planar elliptical solid immersion lens based on a Cartesian oval

D. McCloskey and J. F. Donegan

Citation: Applied Physics Letters **103**, 091101 (2013); doi: 10.1063/1.4818781
View online: http://dx.doi.org/10.1063/1.4818781
View Table of Contents: http://scitation.aip.org/content/aip/journal/apl/103/9?ver=pdfcov
Published by the AIP Publishing

Articles you may be interested in
Mid-infrared imaging with a solid immersion lens and broadband laser source
Appl. Phys. Lett. **90**, 121131 (2007); 10.1063/1.2716337

Direct measurement of laser power through a high numerical aperture oil immersion objective lens using a solid immersion lens
Rev. Sci. Instrum. **73**, 2011 (2002); 10.1063/1.1470231

Near-field photolithography with a solid immersion lens
Appl. Phys. Lett. **74**, 501 (1999); 10.1063/1.123168

Raman imaging of patterned silicon using a solid immersion lens
Appl. Phys. Lett. **73**, 2275 (1998); 10.1063/1.121700

A stroboscopic scanning solid immersion lens microscope
Rev. Sci. Instrum. **68**, 4468 (1997); 10.1063/1.1148416

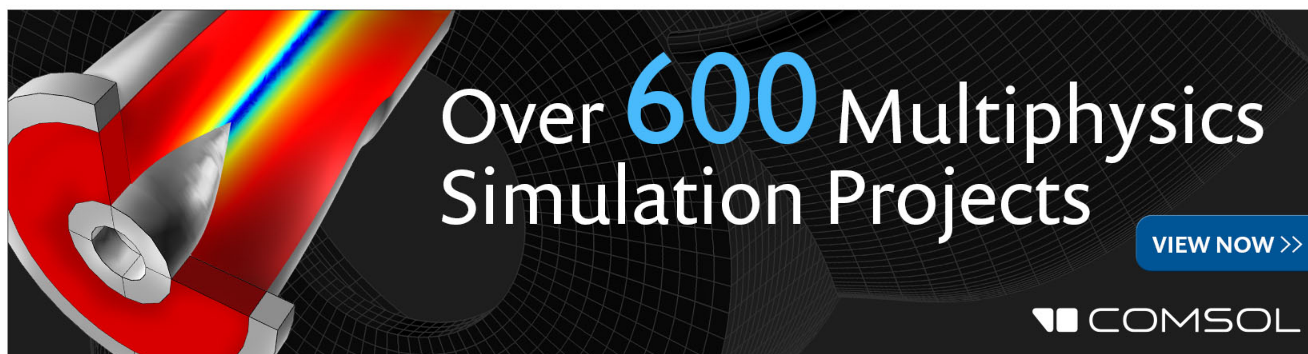

This article is copyrighted as indicated in the article. Reuse of AIP content is subject to the terms at: http://scitation.aip.org/termsconditions. Downloaded to IP: 134.226.93.88 On: Thu, 11 Dec 2014 14:40:09

CrossMark
click for updates

Planar elliptical solid immersion lens based on a Cartesian oval

D. McCloskey[1,2,a)] and J. F. Donegan[1,2]
[1]*School of Physics, Trinity College Dublin, College Green, Dublin 2, Ireland*
[2]*Centre for Research on Adaptive Nanostructures and Nanodevices (CRANN), Trinity College Dublin, College Green, Dublin 2, Ireland*

(Received 12 April 2013; accepted 26 June 2013; published online 26 August 2013)

We report on the design of a single element planar solid immersion lens which is theoretically capable of confining light to a focal spot with full width half maximum of 0.29 λ (154 nm at $\lambda = 532$ nm) and achieving an effective numerical aperture of 1.732. Devices are fabricated and initial optical characterization is performed using a far-field imaging technique providing a lower bound on the numerical aperture of 0.7. Experimental results compare well with two dimensional finite element method simulations. Devices can be mass produced using ultraviolet lithography and produce focal volumes lower than expensive microscope objectives. © *2013 AIP Publishing LLC*. [http://dx.doi.org/10.1063/1.4818781]

The smallest spot that can be produced by focusing propagating light using free space optics is limited to approximately half the wavelength of the incident light by diffraction. Multiple metrics are used to define the diffraction limited spot size. Here, we use the full width half maximum (FWHM) of the square of the Airy function which is given by FWHM $= 0.51\lambda$/NA. The $1/e^2$ waist is calculated from this by $w_{1/e^2} = FWHM\sqrt{\ln(4)}$. This limit results from the finite aperture of the optics which limits the range of spatial frequencies collected. The key to compressing light further is to include higher spatial frequencies.[1] One technique to increase spatial resolution is by taking advantage of evanescent components of the field. Surface plasmon polaritons (SPPs) and localized surface plasmons (LSPs) can confine light to deeply sub-wavelength volumes.[2–4] Aperture scanning techniques such as scanning near field optical microscopy (SNOM) can obtain resolutions of 20 nm by placing a metallic antenna in the near-field of the surface under investigation.[5–7] The efficiency of this technique is however low at 10^{-5} making it unsuitable for excitation and applications which require high throughput.[8] For emerging technologies, such as heat assisted magnetic recording (HAMR), it is necessary to create a small excitation focal volume with high power throughput using a compact device, which can be fabricated using standard lithography techniques.[9]

Solid immersion lenses (SIL) give the possibility to achieve sub-wavelength focal spots while retaining high transmission. An SIL is in general a 3D hemisphere made from a high refractive index material which is placed close to the focal plane of a high NA objective.[10] These structures bend the incident light to effectively increase the NA of the objective. They have been used to achieve a FWHM of 0.25 λ (139 nm @ $\lambda = 560$ nm).[11] There are two traditional designs for solid immersion lenses: a hemispherical lens which increases the resolution by a factor of the refractive index (n)[10] and a super-SIL (Weierstrass geometry) which is capable of increasing the resolution by n^2.[12] These structures are designed to work in conjunction with a high NA focusing lens in order to increase resolution. When the SIL is index matched and brought in contact with the surface, it is referred to as a numerical aperture increasing lens (NAIL) and allows light which would normally be trapped at the surface by total internal reflection to escape to free space. The NAIL has been used to image integrated circuits with a resolution of 0.23 λ (230 nm at $\lambda = 1\ \mu$m).[13] Numerous modifications and optimizations have been made on these designs.[14,15] In practice, it can be difficult to achieve the theoretical resolution for 3D SILs due to polishing imperfections or inaccurate truncation of the sphere.

Planar solid immersion lenses (PSILs) have been proposed as a method to effectively integrate SILs and to alleviate alignment issues.[16,17] Previous work used standard SIL designs, to create PSILs with spot FWHM of 0.71 λ (453 nm at $\lambda = 632.8$ nm).[17] These devices were lossy due to the need for multiple elements. An alternative route is to use reflection instead of refraction. A planar solid immersion mirror (PSIM) was designed which can create a spot size of 0.278 λ (180 nm at 650 nm) and is free from chromatic aberration.[18,19]

Here, we produce a single element planar focusing structure based on refraction capable of producing focal volumes equivalent to a microscope objective of NA = 1.732. The PSIL is fabricated in a 400 nm layer of Si_3N_4 (n = 2.0) deposited by low pressure chemical vapor deposition (LPCVD) on a 2 μm thick thermal oxide SiO_2 (n = 1.4), using electron beam lithography (EBL) and inductively coupled plasma (ICP) etching. The EBL is used in order to facilitate prototyping; however, these structures are large enough to be easily mass produced using UV lithography.

The ideal shape for creating an image without spherical aberration was originally discovered by the famous philosopher and mathematician René Descartes in 1637, then later studied by Newton in 1664 and Maxwell in 1864 and Huygens.[20,21] Specifically the shape can produce two perfectly conjugated planes and is well known in optical lens design[22] as a Cartesian oval. This shape was recently demonstrated to create whispering gallery mode resonators with unidirectional emission.[23]

[a)]mccloskd@tcd.ie

 © 2013 AIP Publishing LLC

This article is copyrighted as indicated in the article. Reuse of AIP content is subject to the terms at: http://scitation.aip.org/termsconditions. Downloaded to IP: 134.226.93.88 On: Thu, 11 Dec 2014 14:40:09

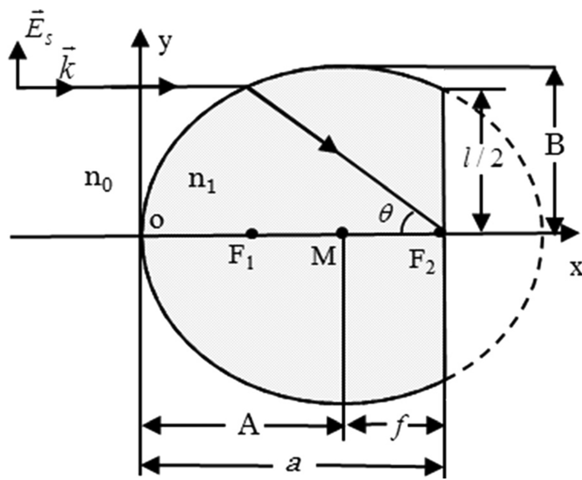

FIG. 1. Schematic of Cartesian oval for focusing collimated light. Truncated region is shaded in grey. Light is indent from the left and focused to a point at F2. F1 and F2 are the foci of the ellipse. The major axis A and minor axis B are shown. The oval is centered at M on the x-axis, with the origin o at the first interface. The parameter l is the length of the chord when the oval is truncated through the second focus. The parameter f is the distance from the center of the oval to the truncated boundary.

For the case of an incident plane wave (i.e., object plane at infinity), the equation of the shape in Cartesian coordinates reduces to

$$\frac{\left(x - a\dfrac{n_1}{n_1 + n_0}\right)^2}{a^2\left(\dfrac{n_1}{n_1 + n_0}\right)^2} + \frac{y^2}{a^2\dfrac{n_1 - n_0}{n_1 + n_0}} = 1. \tag{1}$$

The origin is taken on the centre line of the first boundary of the shape and a is the distance from the origin to the image plane as depicted in Fig. 1. n_1 and n_0 are the refractive index of the ellipse and surrounding material, respectively. Comparison with the standard equation for an ellipse with centre M on the x axis and 0 on the y axis,

$$\frac{(X - M)^2}{A^2} + \frac{Y^2}{B^2} = 1 \tag{2}$$

shows that this describes an ellipse with semi-major axis A, semi-minor axis B, and centre M given by

$$A = \left(\frac{n_1}{n_1 + n_0}\right)a, \tag{3}$$

$$B = \left(\frac{n_1 - n_0}{n_1 + n_0}\right)^{1/2} a, \tag{4}$$

$$M = \left(\frac{n_1}{n_1 + n_0}\right)a. \tag{5}$$

This ellipse has a specific ratio of major to minor axes which depends on the refractive index contrast. The structure thus only depends on one parameter a. These elliptical structures will create a focal spot at F2, which is inside the ellipse. Since the focusing effect occurs completely due to refraction at one interface, the ovals can be truncated at F2 without affecting the NA of the structure. The distance from the centre of the ellipse to the truncated surface f and the length of the chord l are given by

$$f = \left(\frac{n_0}{n_1 + n_0}\right)a, \tag{6}$$

$$l = \left(\frac{2(n_1^2 - n_0^2)}{n_1(n_1 - n_0)}\right)a. \tag{7}$$

For the case of Si_3N_4 in air, $n_1 = 2.0$ and $n_0 = 1$. This leads to $A = 2/3a$, $B = a/\sqrt{3}$, $f = a/3$, and $l = a$. The maximum half angle collected by this structure is $\theta_{max} = 60°$ leading to $NA = n\sin(\theta_{max}) = \sqrt{n^2 - 1} = 1.732$, which is independent of a.

A simple far-field imaging technique depicted in Fig. 2(a) is used to experimentally investigate the focusing

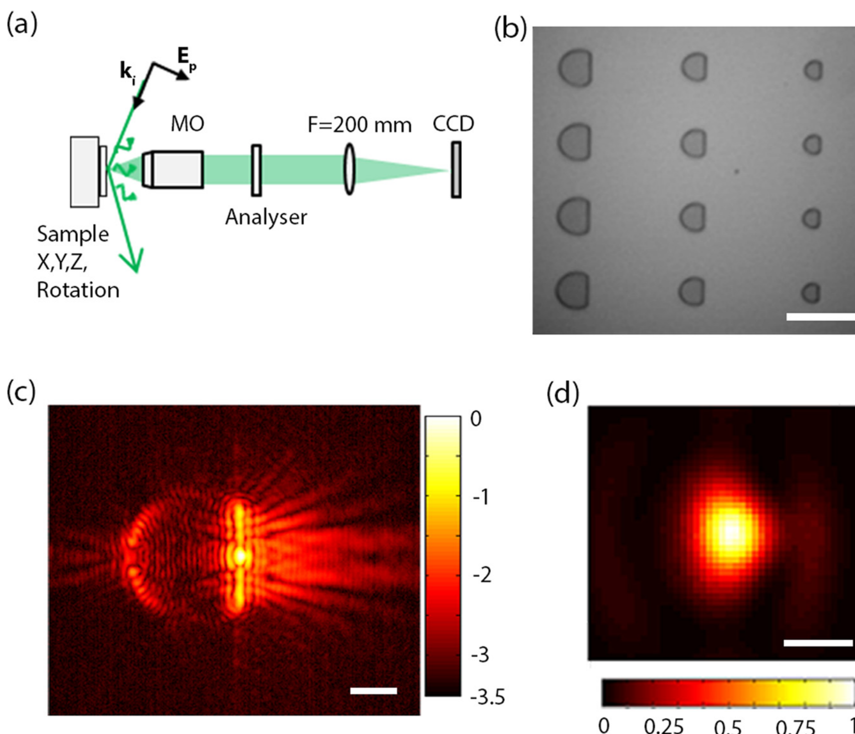

FIG. 2. (a) Experimental setup: Linearly polarized light from a 532 nm DPSS laser is introduced at an angle of 80° to normal. The polarization is controlled to be either s or p polarized with respect to the substrate. The scattered light is collected with a NA = 0.7 100× Mitutoyo long working distance objective and imaged onto a CCD at 100× magnification using a 200 mm focal length lens. (b) Optical micrograph of typical array. Four repeats of $a = 20\,\mu$m, $a = 15\,\mu$m, and $a = 10\,\mu$m are shown. Scale bar: 50 μm. (c) Experimental image on log scale showing near-field intensity distribution. Oval with $a = 10\,\mu$m, incident light p-polarized at 532 nm. Scale bar: 5 μm. (d) Close up of focal spot on linear scale. FWHM of spot size is 420 ± 46 nm, diffraction limited by the collection objective (NA = 0.7). Scale bar: 500 nm.

This article is copyrighted as indicated in the article. Reuse of AIP content is subject to the terms at: http://scitation.aip.org/termsconditions. Downloaded to IP: 134.226.93.88 On: Thu, 11 Dec 2014 14:40:09

properties of these structures. Light from a 3.2 mW CW diode pumped solid state (DPSS) laser with wavelength of 532 nm is incident at 80° to the substrate normal. The beam is spatially filtered to give a Gaussian profile with 1.5 mm $1/e^2$ diameter. This effectively creates a plane wave excitation on the scale of a single scatter. The incident light is controlled to be s-polarized or p-polarized with respect to the substrate. The ovals are imaged from above using a 0.7 NA long working distance microscope objective. Only light which is scattered by the structures into the 45° half angle collection cone of the objective is collected. The resulting image is a spatial map of the origin of the scattered light which is related to the local intensity. Secondary scattering from the SiO_2 substrate creates signal which is two orders of magnitude weaker, giving a map of the local intensity distribution outside of the structure.[24] A linear polarizer can be placed after the objective to analyze the polarisation of the scattered light. A typical array of fabricated structures is shown in Fig. 2(b) under 50× magnification. In order to record signal from both scattering processes, the dynamic range of the CCD is extended by taking four images with different gain and shutter settings and adding them after calibration. An experimental image of a truncated oval with a = 10 μm, $\lambda = 532$ nm, and p-polarized input light is shown on $\log_{10}$ scale in Fig. 2(c). There is detail in the image over 3 orders of magnitude.

A close up of the focal region is shown on a linear scale in Fig. 2(d). The spot is blurred to a FWHM of 420 ± 46 nm by the point spread function (PSF) of the collecting objective (FWHM 390 nm, with NA = 0.7). The near-field intensity distribution is calculated numerically for a 2D structure with the same cross section and an index of 2 using the finite element method (COMSOL). The light is known to be confined to the 400 nm layer in the out of plane direction from previous work[24] putting an upper limit on the spot waist of 200 nm for this case; however, these structures are too large for full 3D numerical simulation. A comparison of numerical results with the experimental images shows that the scattered light retains the polarization properties of the near-field components. Figures 3(a)–3(c) are experimental results with no analyzer and with analyzer polarized along x-axis and y-axis, respectively. The incident light is s-polarized (along y-axis.). Figs. 3(d)–3(f) show the 2D FEM calculated total near-field intensity, $|E_x|^2$ and $|E_y|^2$, respectively. The focal spot is larger for s-polarized light (320 nm) than p-polarized light (154 nm). This is due to the discontinuity of electric field at the interface of the structure in the s-polarized (TE)

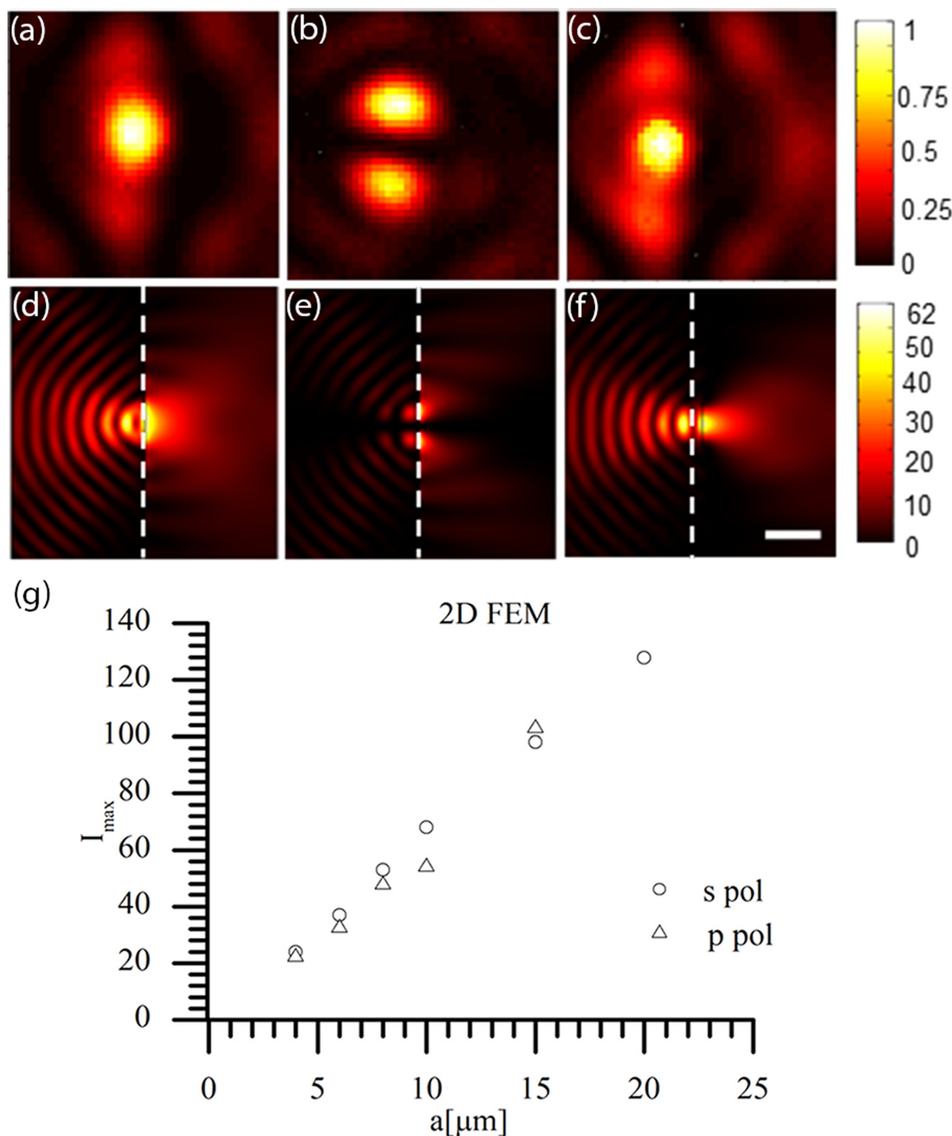

FIG. 3. 2 μm × 2 μm close-up of region around the focus for a truncated oval with $a = 15$ μm. All images are on a linear scale for s-polarized case. The top row figures are normalized experimental measurements with (a) no analyzer, (b) x-polarized, and (c) y-polarized. The second row figures are results of 2D FEM with (d) total field, (e) $|E_x|^2$, and (f) $|E_y|^2$, normalized to the incident intensity. (g) Plot showing linear relationship of focal intensity to a from 2D FEM for both s and p polarized cases.

This article is copyrighted as indicated in the article. Reuse of AIP content is subject to the terms at: http://scitation.aip.org/termsconditions. Downloaded to IP: 134.226.93.88 On: Thu, 11 Dec 2014 14:40:09

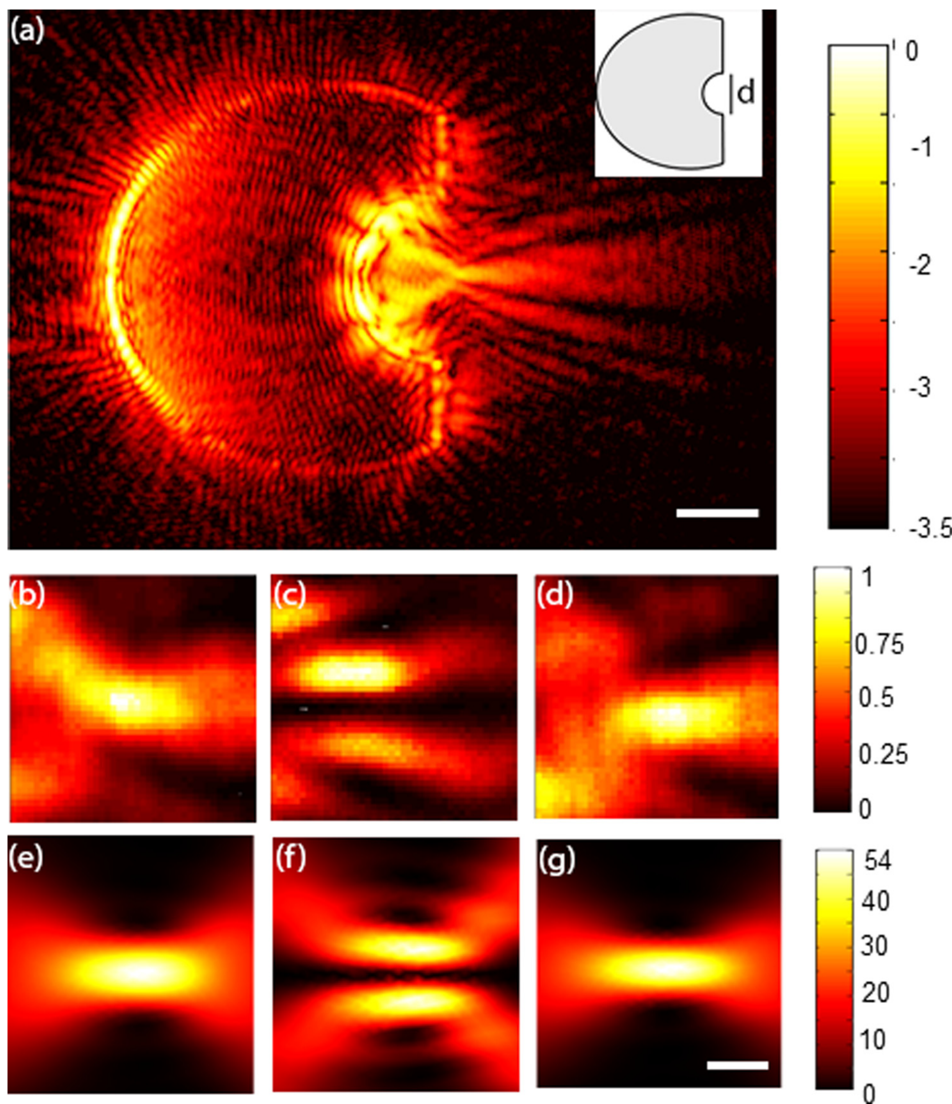

FIG. 4. (a) Experimental image of focusing by a truncated oval with parameter a = 20 μm and a cylindrical cut out with d = 10 μm is shown on log scale. Incident light is s-polarized (along y-axis). Inset showing parameter d. (b) Normalized experimental intensity map for a 2 μm × 2 μm region around the focal region with no analyzer, (c) with analyzer polarized along x-axis, and (d) with analyzer polarized along y-axis. (e) Results of 2D FEM simulation of near field intensity for total field, (f) for x-component $|E_x|^2$, (g) for y-component $|E_y|^2$.

case. The experimental results verify that the PSILs are capable of focusing light at least as tight as a microscope objective with NA = 0.7. Higher resolution methods for mapping the near-field such as SNOM are necessary to see the actual spot size and are currently underway. The intensity enhancement is linear with the parameter a (Fig. 3(g)). Since the focal spot size is independent of a, the structures can be designed for a specific intensity enhancement to suit a particular application.

The Cartesian oval works by converting a plane wave into a cylindrical wave which converges to a point at F2. Since the cylindrical wavefront is created by refraction at the first interface alone, a cylinder with diameter d can be cut into the structure centred on the point F2 as shown inset in Fig. 4. The wavefront will be parallel to this interface and will not undergo refraction, minimising distortion to the focal spot. The oval now acts as a high NA lens with a Gaussian focus outside of the structure which is not in contact with the interface. An experimental image of focusing by a truncated oval with parameter $a = 20\,\mu$m and a cylindrical cut out with $d = 10\,\mu$m is shown on log scale in Fig. 4(a). Controlling the ratio of the diameter of this cut-out to the size parameter of the oval a allows control over the effective NA of the structure and the spot size. The maximum intensity in the focal region I_{max} and the effective NA of the oval calculated from FEM are tabulated for different values of a and d in Table. I. When d is comparable with a, the length of the refracting interface is shortened resulting in a lower NA. When $d < \lambda$, additional confinement results in a higher effective NA.

A design of planar solid immersion lens is presented. The structure is capable of creating an effective NA of

TABLE I. Maximum intensity I_{max} and effective NA tabulated for different a and d.

		a (μm)					
I_{max}/NA		4	6	8	10	15	20
d (μm)	0.2	17/1.65	26/1.54	33/0.89	40/1.7	58/0.95	75/0.89
	0.5	13/0.92	19/0.93	26/0.68	34/0.92	46/0.75	61/0.72
	1	12/0.78	18/0.77	22/0.77	28/0.77	42/0.74	56/0.7
	2	12/0.77	18/0.79	22/0.77	28/0.82	42/0.73	54/0.68
	5	11/0.77	18/0.76	22/0.77	29/0.79	43/0.72	57/0.68
	10		10/0.55	22/0.75	28/0.77	44/0.74	54/0.67

This article is copyrighted as indicated in the article. Reuse of AIP content is subject to the terms at: http://scitation.aip.org/termsconditions. Downloaded to IP: 134.226.93.88 On: Thu, 11 Dec 2014 14:40:09

$\sqrt{n^2-1}$ using a single element and without the need for a focusing lens. These structures are fabricated in Si_3N_4 and shown numerically to produce a focal spot with FWHM of 154 nm at $\lambda = 532$ nm equivalent to an NA of 1.732. A far-field imaging method confirms the spot size is smaller than 420 ± 46 nm (NA = 0.7). Modifying the structure allows access to the focal area and control over the spot size and NA. These structures can be mass produced using standard lithography processes. We have outlined a design to produce these structures in any material system. It is possible to investigate solutions using water as a cladding layer. Use of even higher index materials such as gallium phosphide and shorter wavelengths could produce focal spots with FWHM as small as 87 nm at $\lambda = 560$ nm. (effective NA = 3.27). These devices will find uses as focusing elements for biological sensing, fluorescence correlation spectroscopy (FCS), single molecule excitation, optical recording, optical lithography, and heat assisted magnetic recording. Further work is underway to confirm the spot size using near-field methods and to optimise the materials and thickness of the guiding layer.

The authors would like to thank K. E. Ballantine and P. R. Eastham for useful discussions, and P. Gleeson and N. O'Hara for etching expertise. This work was supported by Science Foundation Ireland (SFI) under Grant No. 08/IN.1/I1862.

[1]L. Novotny and B. Hecht, *Principles of Nano-Optics* (Cambridge University Press, Cambridge, 2006).
[2]L. Feng, K. A. Tetz, B. Slutsky, V. Lomakin, and Y. Fainman, Appl. Phys. Lett. **91**, 081101 (2007).
[3]Z. Liu, J. M. Steele, W. Srituravanich, Y. Pikus, C. Sun, and X. Zhang, Nano Lett. **5**, 1726 (2005).
[4]L. Yin, V. K. Vlasko-Vlasov, J. Pearson, J. M. Hiller, J. Hua, U. Welp, D. E. Brown, and C. W. Kimball, Nano Lett. **5**, 1399 (2005).
[5]H. G. Frey, F. Keilmann, A. Kriele, and R. Guckenberger, Appl. Phys. Lett. **81**, 5030 (2002).
[6]U. Durig, D. W. Pohl, and F. Rohner, J. Appl. Phys. **59**, 3318 (1986).
[7]A. Harootunian, E. Betzig, M. Isaacson, and A. Lewis, Appl. Phys. Lett. **49**, 674 (1986).
[8]L. P. Ghislain, V. B. Elings, K. B. Crozier, S. R. Manalis, S. C. Minne, K. Wilder, G. S. Kino, and C. F. Quate, Appl. Phys. Lett. **74**, 501 (1999).
[9]T. Rausch, C. Mihalcea, K. Pelhos, D. Karns, K. Mountfield, Y. A. Kubota, X. Wu, G. Ju, W. A. Challener, C. Peng, L. Li, Y.-T. Hsia, and E. C. Gage, Jpn. J. Appl. Phys., Part 1 **45**, 1314 (2006).
[10]S. M. Mansfield and G. S. Kino, Appl. Phys. Lett. **57**, 2615 (1990).
[11]Q. Wu, G. D. Feke, R. D. Grober, and L. P. Ghislain, Appl. Phys. Lett. **75**, 4064 (1999).
[12]B. D. Terris, H. J. Mamin, and D. Rugar, Appl. Phys. Lett. **68**, 141 (1996).
[13]S. B. Ippolito, B. B. Goldberg, and M. S. Uünluü, Appl. Phys. Lett. **78**, 4071 (2001).
[14]Y. Zhang, Appl. Opt. **45**, 4540 (2006).
[15]V. V Kotlyar, A. A. Kovalev, and A. G. Nalimov, Optics **1**, 1 (2012).
[16]D. Intani, T. Baba, and K. Iga, Appl. Opt. **31**, 5255 (1992).
[17]D. Chien, C. Tsai, S. Lo, C. Chen, and J. Chang, J. Lightwave Technol. **23**, 2746 (2005).
[18]C. Peng, C. Mihalcea, K. Pelhos, and W. A. Challener, Appl. Opt. **45**, 1785 (2006).
[19]W. A. Challener, C. Mihalcea, C. Peng, and K. Pelhos, Opt. Express **13**, 7189 (2005).
[20]J. P. C. Southall, *Aplanatic (or Cartesian) Optical Surfaces* (J. B. Lippincott, 1922).
[21]R. K. Luneburg, *Mathematical Theory of Optics* (University of California Press, Berkeley, 1964).
[22]D. Michaelis, P. Schreiber, and A. Bräuer, Opt. Lett. **36**, 918 (2011).
[23]Q. J. Wang, C. Yan, N. Yu, J. Unterhinninghofen, J. Wiersig, C. Pflügl, L. Diehl, T. Edamura, M. Yamanishi, H. Kan, and F. Capasso, Proc. Natl. Acad. Sci. U.S.A. **107**, 22407 (2010).
[24]D. McCloskey, J. J. Wang, and J. F. Donegan, Opt. Express **20**, 128 (2012).

This article is copyrighted as indicated in the article. Reuse of AIP content is subject to the terms at: http://scitation.aip.org/termsconditions. Downloaded to IP: 134.226.93.88 On: Thu, 11 Dec 2014 14:40:09